Available online at www.sciencedirect.com
SCIENCE DIRECT®
International Journal of Mass Spectrometry 227 (2003) 47–62
International Journal of Mass Spectrometry
www.elsevier.com/locate/ijms

Sequential bond energies of $Pt^+(NH_3)_x$ ($x = 1$–4) determined by collision-induced dissociation and theory

R. Liyanage[a,1], M.L. Styles[b], R.A.J. O'Hair[b], P.B. Armentrout[a,*]

[a] *Department of Chemistry, University of Utah, Salt Lake City, UT 84112-0850, USA*
[b] *School of Chemistry, University of Melbourne, Parkville, Vic. 3052, Australia*

Received 24 September 2002; accepted 26 October 2002

Dedicated to Rob Dunbar on the occasion of his 60th birthday.

Abstract

The sequential bond energies of $Pt^+(NH_3)_x$ ($x = 1$–4) are determined by collision-induced dissociation (CID) with Xe using guided-ion beam tandem mass spectrometry. Analysis of the kinetic energy-dependent cross sections includes consideration of multiple ion–neutral collisions, the internal energies of the complexes, and the dissociation lifetimes. We obtain the following 0 K bond energies in eV (kJ/mol): 2.84 ± 0.12 (274 ± 12), 2.71 ± 0.10 (261 ± 10), 0.80 ± 0.05 (77 ± 5), and 0.48 ± 0.04 (46 ± 4) for $(NH_3)_{x-1}Pt^+$–NH_3 with $x = 1$–4, respectively. These values are in reasonable agreement with results of density functional ab initio calculations performed here. The trend in these bond energies is compared with those of platinum carbonyl cations and nickel ammonia cation complexes and discussed in terms of sdσ-hybridization, electrostatic interactions, and ligand–ligand steric interactions.

Keywords: Sequential bond energies; Collision-induced dissociation; $Pt^+(NH_3)_x$; Guided ion beam; Metal–ligand complexes; Ab initio calculations

1. Introduction

The square planar cisplatin complex, *cis*-$Pt(NH_3)_2Cl_2$, is used in the treatment of cancer and is one of several $Pt(L)_xCl_y$ species ($x = 1$–3, $y = 1$, 2), where L is a nitrogen-based ligand, that have proven to be of biological importance [1–12]. A number of kinetic and thermodynamic studies have provided insights into the mechanism by which cisplatin exhibits such strong anti-tumor activity [13–16]. Gas-phase studies of cisplatin and cisplatin analogues have generally been limited to the application of mass spectrometric techniques to analyze whether or not these platinum adducts bind to DNA and various proteins [17–23]. We have shown that the collision-induced dissociation (CID) reactions of $[Pt(L_3)M]^{2+}$, and $[Pt(L_3)(M–H)]^+$ (L_3 = 2,2′:6′,2″-terpyridine, diethylenetriamine, and triammonium $(NH_3)_3$); M = amino acid derivatives and simple peptides are dependent on the nature of L_3, M, and the charge state of the ion [24,25]. Despite the many studies conducted in both condensed and gas phases, little is known about the thermodynamics of

* Corresponding author. Tel.: +1-801-581-7885; fax: +1-801-581-8433.
E-mail address: armentrout@chem.utah.edu (P.B. Armentrout).
[1] Present address: State Wide Mass Spectrometry Facility, University of Arkansas, Fayetteville, AR 72701, USA.

1387-3806/03/$ – see front matter © 2003 Elsevier Science B.V. All rights reserved.
doi:10.1016/S1387-3806(03)00050-2

$Pt(NH_3)_xCl_y$ systems, or indeed even simple model systems.

In the present study, we seek to provide such fundamental information by measuring the stepwise energies for dissociation of $Pt^+(NH_3)_x$ (x = 1–4) complexes using guided ion beam mass spectrometry. These are determined by analysis of the kinetic energy dependence of the CID reactions of these complexes with xenon as measured in a guided ion beam tandem mass spectrometer. The data analysis includes consideration of multiple ion–neutral collisions, the internal energies of the complexes, and the dissociation lifetimes. To complement these experimental studies, we also use density functional theory (DFT) calculations to investigate the structures and energetics of these complexes. The approach used here provides a unique opportunity to experimentally probe the *unsaturated* platinum species that could potentially be key intermediates or active agents in reaction pathways of important biological mechanisms [8–10,26–33]. Furthermore, by working in the gas-phase, we are not restricted to stable complexes, a limitation often confronted in solution-phase work.

Previous experimental investigations of the sequential bond dissociation energies of $M^+(NH_3)_x$ (x = 1–4) where M = transition metal have been reported for only the first row transition metal ions (Ti^+–Cu^+) [34–36] and Ag^+ [36]. This previous work included examination of the trends in metal–ligand binding energies resulting from variation of the transition metal center across the period and comparisons to other simple ligand systems, such as CO and H_2O [34]. The present study allows us to examine trends down the periodic table as well as to other ligands, specifically through comparisons with $Ni^+(NH_3)_x$ and $Pt^+(CO)_x$ complexes [34,37].

2. Experimental and theoretical section

2.1. General experimental procedures

The guided-ion beam mass spectrometer on which these experiments were performed has been described in detail previously [38,39]. Briefly, $Pt^+(NH_3)_x$ (x = 1–4) ions are generated in a direct current discharge flow tube source (DC/FT) described below, extracted from the source, accelerated, and focused into a magnetic sector momentum analyzer for mass selection of primary ions. The mass-selected ions are then decelerated to a desired kinetic energy and focused into an octopole ion beam guide that uses radio-frequency electric fields to trap the ions in the radial direction and ensure complete collection of reactant and product ions [40,41]. The octopole passes through a static gas cell with an effective length of 8.26 cm that contains Xe at a low pressure (usually less than ~0.3 mTorr) so that multiple ion–molecule collisions are improbable. The unreacted parent and product ions are confined radially in the guide until they drift to the end of the octopole where they are extracted, focused, and passed through a quadrupole mass filter for mass analysis of products. Ions are subsequently detected with a secondary electron scintillation ion detector using standard pulse counting techniques. Reaction cross sections are calculated from product ion intensities relative to reactant ion intensities after correcting for background signals [42]. Uncertainties in absolute cross sections are estimated to be ±20%.

The kinetic energy of the ions is varied in the laboratory frame by scanning the DC bias on the octopole rods with respect to the potential of the ion source region. Laboratory (lab) ion energies are converted to energies in the center-of-mass frame (CM) by using the formula $E_{CM} = E_{lab}\, m/(m + M)$, where m and M are the neutral Xe and ionic reactant masses, respectively. Two effects broaden the cross section data: the kinetic energy distribution of the reactant ion and the thermal motion of the neutral reactant gas (Doppler broadening) [43]. The absolute zero and the full width at half maximum (fwhm) of the kinetic energy distribution of the reactant ions are determined using the octopole beam guide as a retarding potential analyzer, as described previously [42]. The distributions of ion energies, which are independent of energy, are nearly Gaussian and have a typical fwhm of 0.4–0.8 eV (lab) in these studies. Uncertainties in absolute energy scale are ±0.05 eV (lab).

2.2. Ion source

$Pt^+(NH_3)_x$ ions are produced in a DC/FT source [38], consisting of a cathode held at high negative voltage (1–3 kV) over which a flow of approximately 90% He and 10% Ar passes at a total pressure of 0.3–0.4 Torr and ambient temperature. In this work, the cathode is platinum foil attached to an iron holder. Ar^+ ions created in the discharge are accelerated toward the platinum cathode, thereby sputtering Pt^+. $Pt^+(NH_3)_x$ ions are produced through three-body condensation after NH_3 is introduced into the flow tube 50 cm downstream of the discharge zone. $Pt^+(NH_3)_x$ ions are then swept down the flow tube and undergo $\sim 10^5$ thermalizing collisions with He and $\sim 10^4$ collisions with Ar before entering the guided ion beam apparatus. These collisions with the He/Ar flow gas stabilize and thermalize the ions both rotationally and vibrationally. We assume that these ions are in their ground electronic state and that the internal energy of these clusters is well described by a Maxwell–Boltzmann distribution of rotational and vibrational states corresponding to 300 K, the temperature of the flow tube. Previous studies from this laboratory have shown that these assumptions are consistent with the production of thermalized ions under similar conditions [37,44–49]. Further, we have demonstrated that Pt^+ ions are generated in their $^2D_{5/2}$ ground state under these conditions [50]. Therefore, it seems likely that $Pt^+(NH_3)_x$ ions created under such conditions should also be formed in doublet spin electronic states, the ground states for $x = 1$–4. No obvious evidence for the population of excited electronic states is observed in this work, as described below.

2.3. Data analysis

Several systematic effects influence the ability to derive accurate thermodynamic information from CID thresholds. These effects include (a) multiple collisions with Xe, (b) efficiency of the translational to internal energy transfer, (c) internal excitation of reactant ions that can contribute to the measured thresholds, and (d) the lifetime of the dissociation ions. Here, we account for these factors as follows.

First, our CID experiments were performed under predominantly single collision conditions, as noted above. However, there is always a finite probability of a second collision while the ions go through the collision cell of Xe. Previous CID studies in our laboratory have shown that multiple collisions can strongly affect CID threshold behavior [51–53]. This pressure effect can be eliminated, following a procedure developed previously [53], by linearly extrapolating cross sections measured at different pressures of Xe to zero-pressure, rigorously single collision conditions. It is these linearly extrapolated cross sections that are analyzed for their thresholds. In the present cases, the pressure effects are relatively small with $Pt^+(NH_3)$ and $Pt^+(NH_3)_2$ showing larger effects than $Pt^+(NH_3)_3$ and $Pt^+(NH_3)_4$, an observation that correlates with the relative thresholds observed (higher in the former two cases). Failure to correct for these effects leads to small but systematic lowering of the observed thresholds, in the present cases of about 0.05 eV for the two smaller systems and less for the larger two.

In addition, the choice of collision partner can make a difference in the threshold excitation function [39,51,54–56]. For reasons described in detail previously [39,54,56], we use Xe as the collision partner because it is heavy and polarizable, making the collision more long-lived and hence more efficient at transferring kinetic energy to internal energy of the reactant ions. Some verification of this efficiency comes from direct measurements of energy transfer in the CID of $Cr(CO)_6^+$ with Xe [57]. Experimental distributions of residual kinetic energies are found to extend to zero, the point of 100% energy deposition, indicating that the collisional energy transfer is not impulsive and consistent with transient complex formation.

The internal energy of the reactant ions can contribute to the energy needed to induce dissociation [45,51,56,58]. The flow tube ion source is designed to provide thermalized ions, such that excess vibrational and rotational excitation is unlikely [37,44–49,51]. However, the rotational and vibrational energy of thermalized ions must be considered in the analysis of the

CID thresholds. The internal energy of the ions is best handled by explicitly considering the entire distribution of populated rovibrational states. The model used to reproduce the cross sections of products at zero pressure of Xe is given by Eq. (1) [45,57,59,60],

$$\sigma(E) = \frac{\sigma_0 \sum g_i (E + E_i - E_0)^n}{E} \quad (1)$$

where σ_0 is an energy-independent scaling factor, E is the relative kinetic energy of the reactants, E_0 is the threshold energy for formation of products in their ground rovibrational and electronic states, and n is an adjustable parameter. The sum considers contributions from rovibrational states of the reactant ions, denoted by i, having energies E_i and populations g_i, where $\sum g_i = 1$. We assume that the relative reactivity, as reflected by σ_0 and n, is the same for all rovibrational states. The Beyer–Swinehart algorithm is used to evaluate the density of the rovibrational states of the ions [61–64], and then the relative populations g_i are calculated by the appropriate Maxwell–Boltzmann distribution at 300 K, the temperature of the flow tube. Details about our implementation of this equation are given elsewhere [51,60]. The various sets of vibrational frequencies and rotational constants used to determine E_i in this work are taken from DFT calculations (described below) and are given in Table 1. The electronic energy of the $Pt^+(NH_3)_x$ reactant is believed to be negligible, as noted above. We recently demonstrated that the cross section form given in Eq. (1) is consistent with direct measurements of the energy transferred in collisions between $Cr(CO)_6^+$ with Xe [57]. These results provide increased confidence in the use of Eq. (1) to fit experimental data to obtain accurate thermodynamic information from CID thresholds [57,60,65,66].

We explicitly examine lifetime effects on the thresholds by considering whether or not all ions with energies in excess of the bond energy dissociate within the experimental time window, roughly 10^{-4} s (as determined by time-of-flight measurements) [42,57]. Dissociation of ions is expected to become slower as the size of the complex increases, such that the apparent threshold observed for dissociation can shift to energies higher than the thermodynamic threshold. The lifetime effect is taken into account using Rice–Ramsperger–Kassel–Marcus (RRKM) theory [64,67,68] in the phase space limit (PSL) using equations developed by Rodgers et al. [66]. Briefly, the transition state (TS) for dissociation is modeled by loosely interacting products such that both dissociating fragments are free to rotate. This PSL is appropriate for ion–molecule complexes because the TS for the reverse, barrierless association process is accurately described as lying at the top of

Table 1
Vibrational frequencies and rotational constants of $Pt^+(NH_3)_x$ (x = 1–4)[a]

Structure	Zero point energies (eV)	Vibrational frequencies (cm^{-1})	Rotational constants (cm^{-1})
NH_3	0.9392	1062.3, 1715.2, 1715.9, 3460.8, 3597.6, 3598.9	9.924 (2), 6.188
$Pt^+(NH_3)$	1.0768	470.6, 830.5, 830.8, 1402.9, 1685.2, 1686.5, 3421.3, 3520.8, 3521.6	6.101, 0.232 (2)
$Pt^+(NH_3)_2$	2.1754	21.9, 166.2, 166.9, 468.6, 471.9, 757.3, 759.1, 817.5, 818.8, 1397.3, 1397.8, 1703.6, 1704.4, 1706.1, 1706.6, 3439.7, 3441.0, 3535.9, 3536.2, 3537.0, 3537.1	3.100, 0.103 (2)
$Pt^+(NH_3)_3$	3.2093	36.7, 57.9, 63.3, 108.5, 164.2, 166.8, 293.0, 433.2, 438.7, 547.3, 556.6, 709.0, 728.0, 776.1, 777.6, 1264.0, 1366.6, 1368.1, 1699.2, 1701.9, 1703.2, 1711.9, 1715.7, 1717.4, 3445.2, 3445.9, 3452.8, 3541.3, 3541.6, 3546.5, 3547.3, 3571.5, 3572.9	0.167, 0.101, 0.0648
$Pt^+(NH_3)_4$	4.1919	32.7, 63.9, 66.3, 80.7, 94.7, 109.0, 125.9, 137.0, 152.8, 165.2, 205.2, 380.0, 391.5, 401.2, 431.0, 444.5, 447.9, 651.7, 678.8, 713.4, 722.2, 1221.7, 1223.3, 1328.2, 1329.2, 1701.0, 1705.9, 1707.1, 1709.8, 1714.8, 1715.4, 1717.4, 1728.8, 3447.1, 3447.4, 3453.1, 3453.4, 3554.5, 3555.0, 3560.3, 3560.5, 3570.8, 3571.1, 3574.3, 3574.4	0.0953, 0.0726, 0.0424

[a] Calculated at the B3LYP/(HWRECP/6-31+G*) level. All values are unscaled.

the centrifugal barrier. In this study, the 2-D external rotations are treated adiabatically but with centrifugal effects included, consistent with the discussion of Waage and Rabinovitch [69]. The adiabatic 2-D rotational energy is treated using a statistical distribution with explicit summation over the possible values of the rotational quantum number, as described in detail elsewhere [66]. The vibrational frequencies of the reactants and transition states are taken from the DFT calculations detailed below and are listed in Table 1.

Before comparison with the experimental data, Eq. (1) is convoluted with the kinetic energy distributions of the reactant ions and Xe at 300 K. The σ_0, n, and E_0 parameters are then optimized using a nonlinear least-squares analysis to give the best reproduction of the data [42]. Error limits for E_0 are calculated from the range of threshold values for different datasets over a range of acceptable n values, from a variation of ±25% for the vibrational frequencies, and from the absolute uncertainty in the energy scale.

Because the vibrational, rotational, and translational energy distributions of the reactants are explicitly included in our modeling, the E_0 thresholds obtained here correspond to 0 K values. We take these thresholds to equal $D_0[(NH_3)_{x-1}Pt^+–NH_3]$, implicitly assuming that there are no activation energies in excess of the endothermicities for dissociation, i.e., there are no reverse activation barriers. This assumption is reasonable for ion–molecule reactions because of the long-range ion-induced dipole and ion–dipole attractive potential [45,60,66]. In addition, theoretical considerations demonstrate that potential energy surfaces for heterolytic bond dissociations, such as those considered here, should have no intrinsic barriers [70]. An experimental study of the kinetic energy release distributions of the decomposition of $Mn(CO)_x^+$ complexes have demonstrated that this is correct for metal carbonyl species [71]. Curve crossings with surfaces of different spin could alter this situation, but all of the $Pt^+(NH_3)_x$ complexes considered here have doublet spin ground states. No low lying excited electronic states of the $Pt^+(NH_3)_x$ species are expected and no evidence for such states is observed here.

2.4. Computational procedures

DFT calculations [72,73] based on the hybrid gradient-corrected exchange functional proposed by Becke [74] combined with the gradient-corrected correlation functional of Lee et al. [75], commonly known as B3LYP functional, were carried out with the GAUSSIAN 98 suite of programs [76]. The DFT method based on the hybrid B3LYP functional has been shown to be a better approach to model binding energies of transition metal atoms compared to classical HF methods [74]. Scott and Radom [77] have shown that B3LYP harmonic vibrational frequencies reproduce observed fundamentals with good accuracy. In this work, full geometry optimizations and vibrational frequencies were performed using a hybrid basis set where Pt was treated with the LANL2DZ basis set, which uses the Hay-Wadt VDZ ($n + 1$) relativistic effective core potential (RECP) [78], and the 6-31+G* basis set was used for N and H atoms. For convenience, we will refer to this hybrid basis set as (HWRECP/6-31+G*). Vibrational analyses were performed on all optimized geometries to verify that they represent minima on the potential energy surface. Vibrational frequencies and rotational constants obtained (Table 1) were used for thermochemical analysis of the experimental cross sections as detailed above. Using these geometries, single point energy calculations were performed using the expanded 6-311+G* basis set on N and H atoms, and the LANL2DZ basis set on Pt, referred to as (HWRECP/6-311+G*). To verify the accuracy of the theoretical bond energies, geometries were reoptimized using a larger basis set on N and H (HWRECP/6-311+G**) and then single point energies calculated using HWRECP/6-311++G(3df,3p). Zero point energy corrections to the theoretical energies at both levels used the vibrational frequencies calculated at the HWRECP/6-31+G* level and scaled by 0.9804 [79].

In calculating bond energies from the theoretical absolute energies, it is important to realize that these calculations do not explicitly include spin–orbit interactions. Therefore, calculations involving dissociation to Pt^+ are referenced to the weighted average energy

of the spin–orbit components of the ^{2}D term, which lies at 0.418 eV experimentally [50,80]. To properly compare to experimental values, which are referenced to the energy of the $^2D_{5/2}$ ground state at 0.0 eV, the calculated value must be corrected for this different asymptotic energy.

3. Experimental and theoretical results

Results for the interactions of $Pt^+(NH_3)_x$ with Xe as a function of collision energy are shown in Figs. 1–4 for $x = 1$–4. In all cases, the major product is formed in the simple CID process (reaction (2)).

$$Pt^+(NH_3)_x + Xe \rightarrow Pt^+(NH_3)_{x-1} + NH_3 + Xe \quad (2)$$

At higher energies, additional ammonia ligands can be eliminated in what is apparently a sequential process. This is most evident in the data for $Pt^+(NH_3)_4$ where it can be seen that the cross section for the primary $Pt(NH_3)_3^+$ product ion declines as the secondary $Pt^+(NH_3)_2$ product ion is formed. The thermochemistry derived below further is consistent with the apparent thresholds observed, as discussed below, thereby verifying the sequential nature of the dissociations. No appreciable $(NH_3)_xPt^+Xe$ (x = 1–3) products formed by ligand exchange reactions were observed. We also looked for $HPt^+(NH_3)_{x-1}$ products but did not observe these, however, such products almost certainly have higher threshold energies than elimination of intact ammonia molecules such that they may be difficult to observe compared to $Pt^+(NH_3)_{x-1}$ products, which should be much more intense. Similarly, observation of $(NH_2)Pt^+(NH_3)_{x-1}$ or $(NH)Pt^+(NH_3)_{x-1}$ is very difficult because of the intensity of the nearby reactant ion beam.

It is obvious from the cross sections that the thresholds for loss of ammonia from the $x = 1$ and 2 complexes lie above 2 eV, whereas those for $x = 3$ and 4 are substantially lower in energy. Indeed, the apparent thresholds of these latter ligands are essentially 0 eV. This trend is also reflected in the thresholds for the secondary products observed for $x = 2$–4 and for the tertiary $Pt^+(NH_3)$ product observed for $x = 4$.

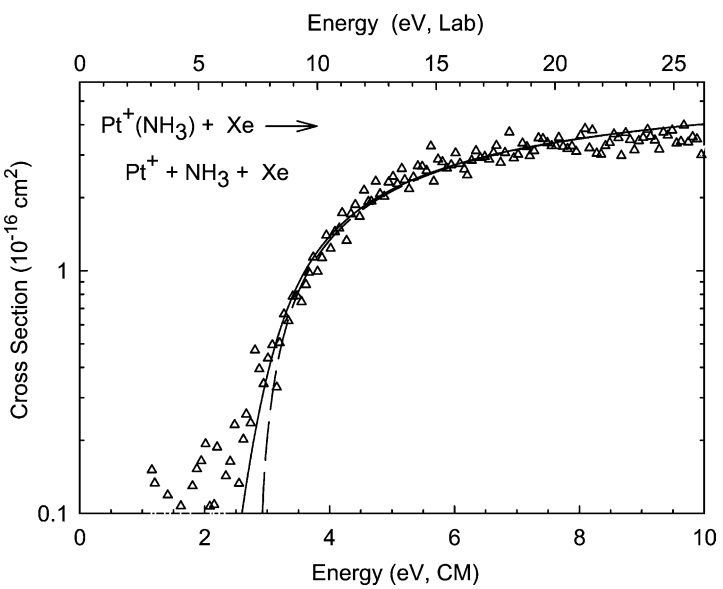

Fig. 1. Zero pressure extrapolated cross sections for the reaction of $Pt^+(NH_3)$ with Xe as a function of kinetic energy in the center-of-mass frame (lower x-axis) and laboratory frame (upper x-axis) to form Pt^+ (open triangles). The dashed line is a model of the CID cross section that uses Eq. (1) with the parameters in Table 2 for 0 K reactants, and the solid line is the same model convoluted over the translational and rovibrational energy distributions of reactants.

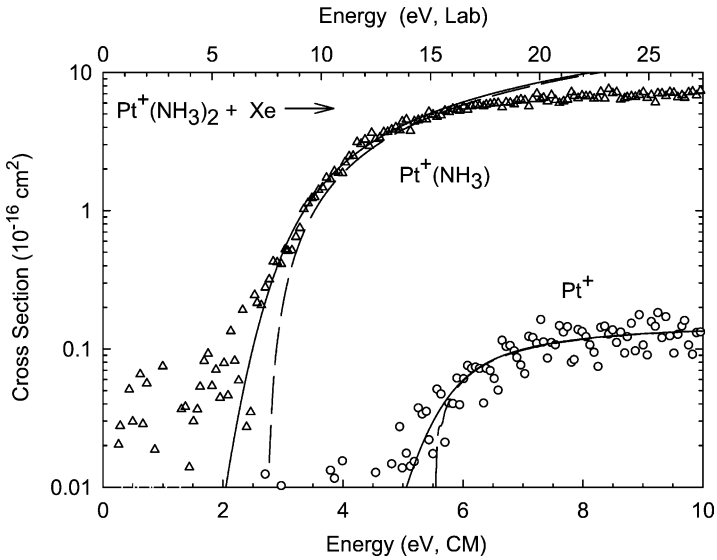

Fig. 2. Zero pressure extrapolated cross sections for the reaction of $Pt^+(NH_3)_2$ with Xe as a function of kinetic energy in the center-of-mass frame (lower *x*-axis) and laboratory frame (upper *x*-axis) to form $Pt^+(NH_3)$ (open triangles) and Pt^+ (open circles, multiplied by a factor of 10). The dashed lines are models of the CID cross sections that use Eq. (1) with the parameters in Table 2 for 0 K reactants, and the solid lines are the same models convoluted over the translational and rovibrational energy distributions of reactants.

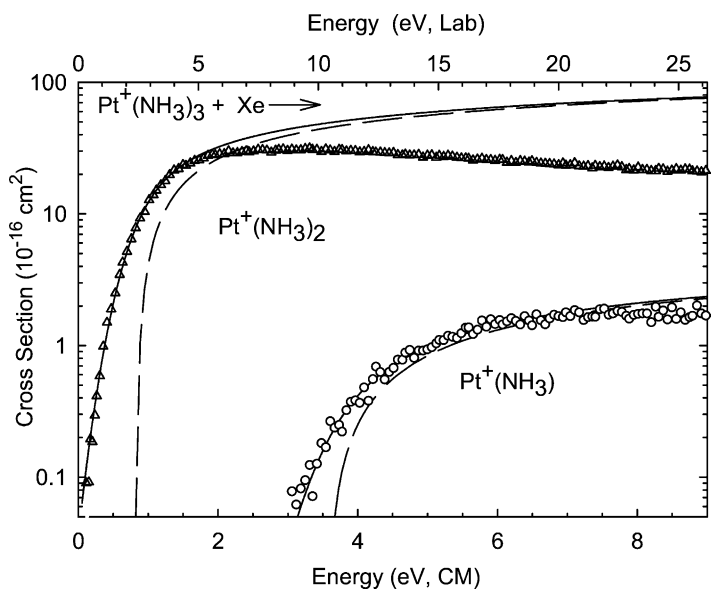

Fig. 3. Zero pressure extrapolated cross sections for the reaction of $Pt^+(NH_3)_3$ with Xe as a function of kinetic energy in the center-of-mass frame (lower *x*-axis) and laboratory frame (upper *x*-axis) to form $Pt^+(NH_3)_2$ (open triangles) and $Pt^+(NH_3)$ (open circles). The dashed lines are models of the CID cross sections that use Eq. (1) with the parameters in Table 2 for 0 K reactants, and the solid lines are the same models convoluted over the translational and rovibrational energy distributions of reactants.

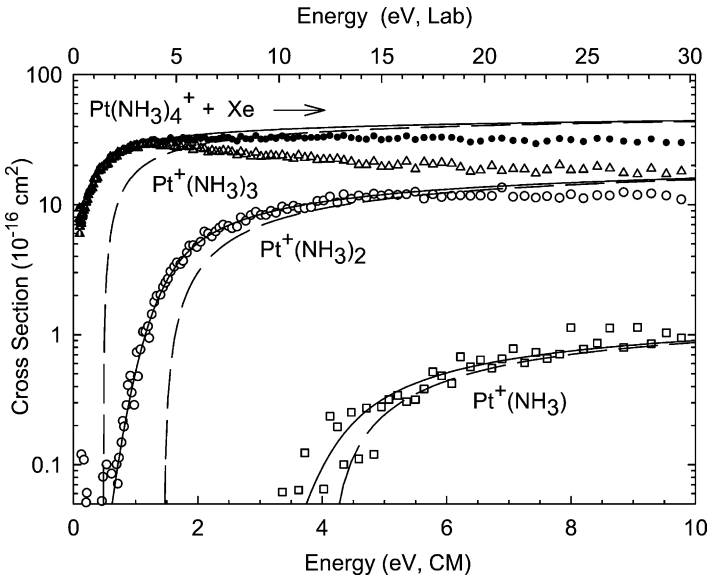

Fig. 4. Zero pressure extrapolated cross sections for the reaction of $Pt^+(NH_3)_4$ with Xe as a function of kinetic energy in the center-of-mass frame (lower *x*-axis) and laboratory frame (upper *x*-axis) to form $Pt^+(NH_3)_3$ (open triangles), $Pt^+(NH_3)_2$ (open circles), and $Pt^+(NH_3)$ (open squares). The total cross section is indicated by the small solid circles. The dashed lines are models of the CID cross sections that use Eq. (1) with the parameters in Table 2 for 0 K reactants, and the solid lines are the same models convoluted over the translational and rovibrational energy distributions of reactants.

Absolute cross sections increase with increasing ligation reaching maximum cross sections of about 3, 7, 30, and 30 Å^2 for $x = 1$–4, respectively. These maxima reflect the changing thresholds, the number of ligands available for dissociation, and the size of the complex. Cross sections for the secondary and tertiary product ions are 1–2 orders of magnitude smaller than those of the primary dissociation channel.

3.1. BDEs from primary thresholds

As concluded in our previous CID experiments, our best measurement of the bond dissociation energies for metal–ligand complex ions comes from analysis of the primary dissociation channels (reaction (2)). These are the least susceptible to the effects of kinetic shifts, competition with other channels, and

Table 2
Optimized parameters of Eq. (1) for CID of $Pt^+(NH_3)_x$ ($x = 1$–4) complexes with Xe

Reactant	Products	σ_0	n	E_0 (eV)[a]	E_0 (PSL) (eV)	E_0 (sum)[b] (eV)
$Pt(NH_3)^+$	$Pt^+ + NH_3$	6.0 ± 1.3	1.1 ± 0.1	2.92 ± 0.06	2.84 ± 0.12	
$Pt(NH_3)_2^+$	$Pt^+(NH_3) + NH_3$	5.0 ± 1.3	1.6 ± 0.3	2.78 ± 0.05	2.71 ± 0.10	
	$Pt^+ + 2NH_3$	0.5 ± 0.1	0.7 ± 0.1	5.70 ± 0.13	5.50 ± 0.20	5.55 ± 0.16
$Pt(NH_3)_3^+$	$Pt^+(NH_3)_2 + NH_3$	43.2 ± 3.1	1.1 ± 0.2	0.82 ± 0.03	0.80 ± 0.05	
	$Pt^+(NH_3) + 2NH_3$	4.4 ± 1.4	1.3 ± 0.2	3.65 ± 0.04	3.57 ± 0.06	3.51 ± 0.11
$Pt(NH_3)_4^+$	$Pt^+(NH_3)_3 + NH_3$	36.0 ± 2.1	1.0 ± 0.1	0.52 ± 0.02	0.48 ± 0.04	
	$Pt^+(NH_3)_2 + 2NH_3$	18.0 ± 1.0	1.2 ± 0.3	1.46 ± 0.07	1.37 ± 0.12	1.28 ± 0.06
	$Pt^+(NH_3) + 3NH_3$	1.0 ± 0.2	1.2 ± 0.1	4.20 ± 0.06	4.00 ± 0.10	3.99 ± 0.12

[a] Values obtained without including an analysis of the kinetic shifts.
[b] Sum of primary threshold energies.

multiple collisions. Listed in Table 2 are the optimized parameters of Eq. (1) obtained from the analyses of reaction (2) for the $Pt^+(NH_3)_x$ (x = 1–4) systems. These models are shown in Figs. 1–4, and can be seen to reproduce the data well in the threshold regions. The σ_0 and E_0 values properly reflect the relative magnitudes and thresholds noted above. We find that lifetime effects are fairly small, about 0.08 eV for $Pt^+(NH_3)$ and $Pt^+(NH_3)_2$ and smaller, about 0.03 eV, for $Pt^+(NH_3)_3$ and $Pt^+(NH_3)_4$, well within our experimental errors. Although kinetic shifts might be anticipated to be larger for the larger complexes, this effect is overwhelmed by the change in threshold energies such that smaller shifts occur for the more weakly bound species.

Also shown in Figs. 1–4 and in Table 2 are analyses of the secondary and tertiary products. Kinetic shifts for these processes are somewhat larger than for the primary decomposition processes, as much as 0.2 eV, largely because the thresholds are higher. The thresholds for these higher energy reactions compare well with those calculated from the primary threshold energies (Table 2), providing additional confidence in the accuracy of the BDE assignments. It might be noted, however, that such agreement is the exception rather than the rule as secondary thresholds are generally higher than those calculated from the primary thresholds for metal ligand systems [37,51,81].

3.2. Theoretical results

The fully optimized ground state geometries for all $Pt^+(NH_3)_x$ (x = 1–4) structures calculated at the B3LYP/(HWRECP/6-311+G**) level of theory are shown in Fig. 5. Table 3 provides several key bond lengths and bond angles. In all cases, the ammonia ligands orient the nitrogen lone pair electrons to point at the platinum ion, such that the dipole moment of ammonia is aligned with the bond axis. The N–H bonds of ammonia lengthen upon complexation to Pt^+, and the extent of this elongation decreases slightly with increasing ligation. The Pt–N bond length in the mono-ligated complex, $Pt^+(NH_3)$, is sensitive to the size of the basis set used, whereas larger complexes show less sensitivity. Pt–N bond lengths increase with increasing ligation and for the x = 3 and 4 complexes, there are two short Pt–N bonds and one or two long bonds, respectively. The mono-ligated complex has C_{3v} symmetry, whereas the bis-ligated complex has D_{3h} symmetry, a consequence of the linear N–Pt–N

Table 3
Structures of $Pt^+(NH_3)_x$ (x = 1–4)[a]

Structure	Symmetry	r(Pt–N) (Å)	r(N–H) (Å)	∠[N–Pt–N] (degrees)
NH_3	C_{3v}		1.014 (3), *1.014 (3)* 1.014 (3)	
$Pt^+(NH_3)$	C_{3v}	2.063, *2.048*, 2.036	1.025 (3), *1.022 (3)* 1.020 (3)	
$Pt^+(NH_3)_2$	D_{3h}	2.100 (2), *2.100 (2)*	1.023 (6), *1.020 (6)*	179.9, *180.0*
$Pt^+(NH_3)_3$	C_s	2.115 (2), *2.118 (2)* 2.325, *2.341*	1.022 (6), *1.019 (6)* 1.020 (3), *1.017 (3)*	94.6 (2), *94.6 (2)* 170.8, *170.8*
$Pt^+(NH_3)_4$	C_{2h}	2.152 (2), *2.154 (2)* 2.492 (2), *2.513 (2)*	1.020 (6), *1.017 (8)* 1.021 (4), *1.018 (4)* 1.022 (2)	89.8 (2), *89.0 (2)* 90.2 (2), *91.0 (2)* 179.2[b], *180.0* 178.1[c], *180.0*

[a] Values in roman are calculated at the B3LYP/(HWRECP/6-31+G*) level. Values in italics are calculated at the B3LYP/(HWRECP/6-311+G**) level. Underlined values are calculated at the B3LYP/(HWRECP/6-311++G(3df,3p)) level.
[b] Angle between short Pt–N bonds.
[c] Angle between long Pt–N bonds.

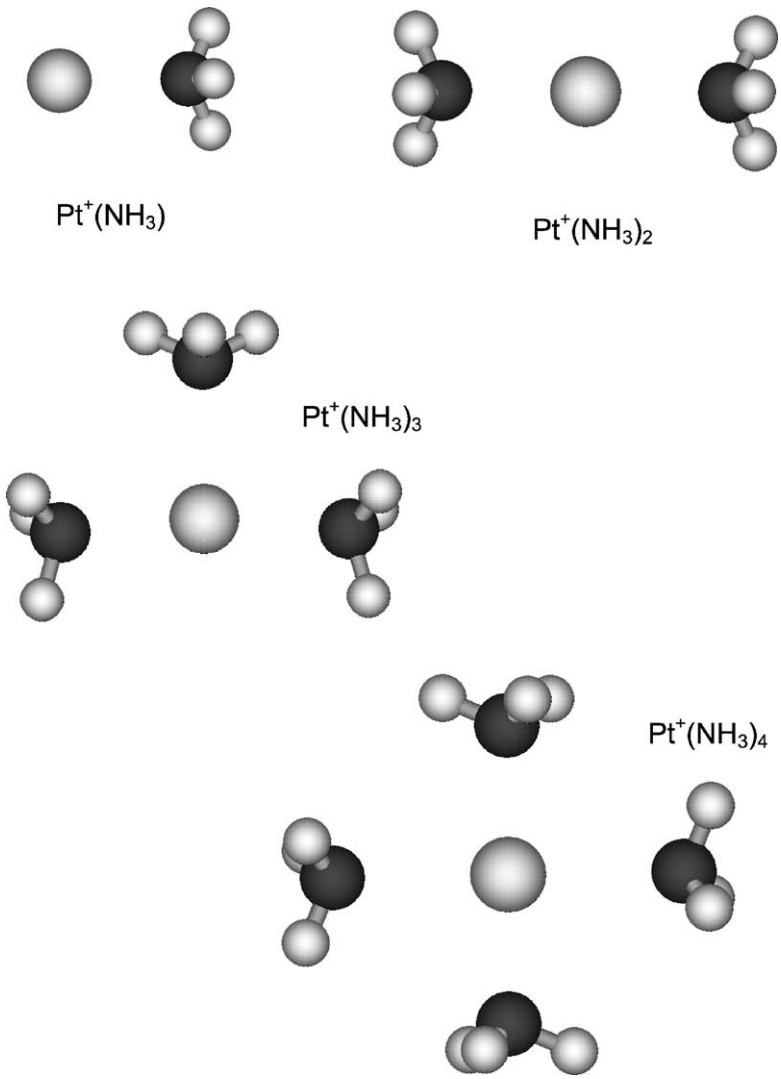

Fig. 5. Structures of the $Pt^+(NH_3)_x$ complexes calculated at the B3LYP/(HWECP/6-311+G**) level.

bond angle. In $Pt^+(NH_3)_2$, rotation of one of the ammonia ligands by 60° yields a complex having D_{3d} symmetry, which is calculated to lie less than 1 meV higher in energy, illustrating that the rotation of the ammonia ligands is essentially free. In the $Pt^+(NH_3)_3$ complex, the two short Pt–N bonds are located 170.8° apart, a distortion from a linear arrangement clearly induced by repulsion with the third ammonia ligand. In both the $x = 3$ and 4 complexes, the sum of the N–Pt–N bond angles is 360°, indicating that the Pt and N atoms are coplanar (within 1°). In the tetra-ligated complex, both the two short Pt–N bonds and the two long Pt–N bonds have angles of 180.0°; however, the angles between the short and long bonds are not 90°, but 91° and 89°. This appears to be a result of repulsion between the ammonia ligands at short distances with the hydrogens that lie in the plane of the molecule and are on the adjacent ammonia ligand. A similar

Table 4
Absolute energies and bond dissociation energies for $Pt^+(NH_3)_x$ ($x = 1$–4) complexes

Structure	Spin	Energy[a] (h)	$D_0[(NH_3)_{x-1}Pt^+–NH_3]$ (eV)	
			Theory	Experimental
Pt^+	2	−118.735491		
NH_3	1	−56.538985 *−56.553012* −56.553074		
$Pt^+(NH_3)$	2	−175.388362 *−175.405158* −175.405233	2.681[b] *2.756*[b] 2.757[b]	2.84 ± 0.12
$Pt^+(NH_3)_2$	2	−232.028342 *−232.054003*	2.748 *2.607*	2.71 ± 0.10
$Pt^+(NH_3)_3$	2	−288.606131 *−288.638204*	1.056 *0.849*	0.80 ± 0.05
$Pt^+(NH_3)_4$	2	−345.159515 *−345.202107*	0.392 *0.296*	0.48 ± 0.04

[a] Single point energies calculated at the B3LYP/(HWRECP/6-311+G*)//B3LYP/(HWRECP/6-31+G*) level. Values in italics are calculated at the B3LYP/(HWRECP/6-311++G(3df,3p)//B3LYP/(HWRECP/6-311+G**) level. Underlined values are calculated at the B3LYP/(HWRECP/6-311++G(3df,3p))//B3LYP/(HWRECP/6-311++G(3df,3p)) level. All values include zero point energy corrections (scaled by 0.9804) calculated at the B3LYP/(HWRECP/6-31+G*) level (Table 1).

[b] Values include correction for the experimental spin orbit splitting energy of Pt^+, 0.418 eV (see text).

interaction is present in the other pair of ligands (NH_3 at long distances with hydrogens on adjacent ligands) but is apparently slightly less repulsive because of the difference in Pt–N bond lengths.

Table 4 lists the theoretically predicted absolute energies for minima located on the $Pt^+(NH_3)_x$ ($x = 1$–4) potential energy surface calculated at the B3LYP/(HWRECP/ 6- 311+G*)/ B3LYP/(HWRECP/6-31+G*) and B3LYP/(HWRECP/6-311++G(3df,3p))//B3LYP/(HWRECP/6-311+G**) levels of theory. All values have been corrected for zero point energies, listed in Table 1, after scaling by 0.9804 [79]. Adiabatic bond dissociation energies have been calculated from the absolute energies and are also listed in Table 4. Basis set superposition error (BSSE) corrections have not been carried out, in part because they are expected to be small for the relatively large basis sets used here and for B3LYP calculations [82].

As shown in Table 4, the theoretical results reproduce the general trends in the experimental bond energies, namely that the first two ligands are bound strongly, whereas the third and fourth ligand binding energies are much weaker. The differences between the theoretical and experimental values are comparable to the experimental uncertainties and vary from 0.04–0.26 eV for the B3LYP/(HWRECP/6-311+G*)//B3LYP/(HWRECP/6-31+G*) calculations and 0.05–0.18 eV for the B3LYP/(HWRECP/6-311++G(3df,3p))//B3LYP/(HWRECP/6-311+G**) calculations. The overall quantitative agreement is quite good with a mean absolute deviation (MAD) of 0.14 ± 0.09 eV and a mean signed deviation (MSD) of 0.01 ± 0.18 eV for the smaller basis set results. The latter indicates that the sum of the four bond energies is quite accurately predicted, 6.83 ± 0.17 eV found experimentally vs. 6.88 eV found theoretically. For the larger basis sets, the MAD is 0.11 ± 0.06 eV and the MSD is 0.08 ± 0.10 eV, with a bond energy sum of 6.51 eV. Note that the values obtained with the larger basis sets correctly predict that the $Pt^+–NH_3$ bond energy is larger than that for $(NH_3)Pt^+–NH_3$ by 0.15 eV, compared to the experimental difference of 0.13 eV. In contrast, the results from the smaller basis sets invert the order of these two bond energies.

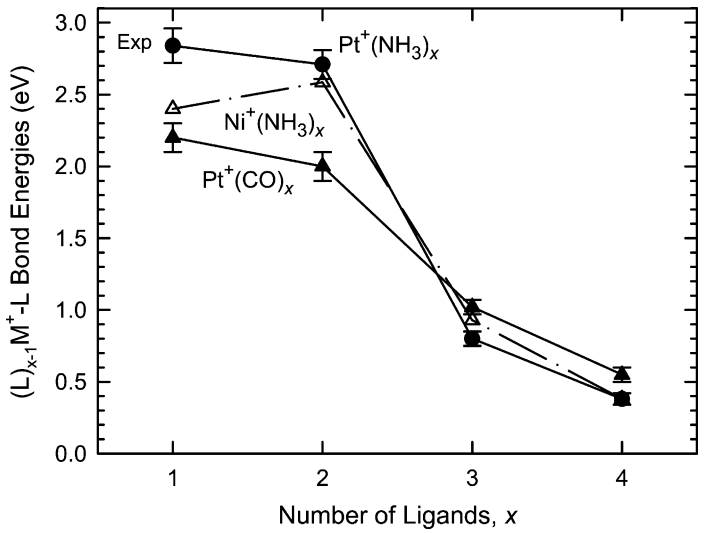

Fig. 6. Bond energies for loss of one ligand from $Pt^+(NH_3)_x$ (solid circles), $Ni^+(NH_3)_x$ (open triangles) [34], and $Pt^+(CO)_x$ (closed triangles) [37] as a function of the number of ligands. Error bars are indicated for the experimental BDEs of $Pt^+(NH_3)_x$ and $Pt^+(CO)_x$.

4. Discussion

4.1. Sequential BDEs of $Pt^+(NH_3)_x$

Because of the attractive charge-induced dipole and charge–dipole interactions between a metal ion (M^+) and neutral ligands (L), the starting point for thinking about the bonding in M^+L_x species is electrostatics. If there is no change of electronic structure on M^+ upon ligation, then the bond energies of M^+L_x can be expected to decrease monotonically with the number of ligands. This is a result of the declining effective charge on the metal as more ligands are attached and increasing repulsive interactions between ligands that become more sterically crowded. Alkali metal complexes behave in this way because of the closed shell electronic structure for M^+ [55,83,84]. In all four $Pt^+(NH_3)_x$ complexes as well as Pt^+, the ground electronic states have doublet spin, such that all dissociation processes examined here are spin-allowed. Therefore, it is not surprising that the sequential BDEs of $Pt^+(NH_3)_x$ decrease with the number of NH_3 ligands (Fig. 6). However, the Pt^+–NH_3 and $(NH_3)Pt^+$–NH_3 BDEs are much stronger than those for $Pt^+(NH_3)_x$ ($x = 3$ and 4). This trend in sequential BDEs can be explained using sdσ-hybridization [34,65,85–88]. The first NH_3 ligand induces hybridization of the empty 6s orbital on $Pt^+(^2D,5d^9)$ with the singly occupied 5dσ orbital directed along the bonding axis. Because the ground state of Pt^+ is $^2D(5d^9)$, no promotion energy is needed for sdσ-hybridization. This hybridization effectively removes electron density from the metal–ligand axis by placing the electron density in a sdσ hybrid orbital that is largely perpendicular to this axis. This allows a shorter bond length and an enhancement of the electrostatic interaction between Pt^+ and the NH_3 ligand. Because of the symmetry of the sdσ hybrid orbitals, electron density is removed along the bonding axis on both sides of the metal. Thus, a second NH_3 ligand located 180° from the first NH_3 ligand can also bind strongly to Pt^+ while keeping ligand–ligand interactions to a minimum. Consequently, the BDE of the second ligand is nearly as strong as the first (Table 4). Indeed, our DFT calculations find that $Pt^+(NH_3)_2$ has a linear N–Pt–N arrangement (Table 3). The Pt–N bond lengths in the bis-ligated complex are longer (2.100 Å) than those in the mono-ligated complex (2.048 Å), consistent with slightly weaker binding for the second ligand. Calculations indicate that the singly

occupied molecular orbital (SOMO) is indeed an sdσ hybrid where the electron density is perpendicular to the N–Pt–N bond axis.

Because of the symmetry of sdσ hybrids, a third NH_3 ligand cannot bind as strongly as the first two ligands. If hybridization is lost completely, then a trigonal planar geometry with N–Pt–N bond angles of 120° is expected. In contrast, DFT calculations find a distorted trigonal planar structure (C_s symmetry) which is nearly T-shaped for $Pt^+(NH_3)_3$ in which the N–Pt–N bond angles are 170.8°, 94.6°, and 94.6°. The ammonia in the middle position (Fig. 5) has a longer Pt–N bond length, 2.341 Å vs. 2.118 Å for the other two ligands. The latter bonds are slightly longer than those in the bis-ligated complex. Thus, most of the effects of the sdσ-hybridization are retained by the two strongly bound ligands, leaving a third weakly binding ligand interacting with the electron density in the other sdσ hybrid. Indeed examination of the molecular orbitals shows that the singly occupied molecular orbital (the SOMO) is antibonding between the Pt and the weakly bound NH_3 ligand. This orbital is polarized away from the ligand, indicating that the SOMO has some 6p character, like in similar situations calculated for $Co(H_2)_3^+$ [89] and $Co(CH_4)_3^+$ [90]. The sp-hybridization costs more energy than sdσ-hybridization and therefore is not as effective.

Calculations indicate that $Pt^+(NH_3)_4$ has a near-planar structure (less than 1° deviation) among the four nitrogen atoms and Pt. There are two short Pt–N bond lengths of 2.154 Å, somewhat elongated from the smaller clusters, and two long Pt–N bond lengths of 2.514 Å, much longer than the long Pt–N bond in the $Pt^+(NH_3)_3$ complex. The N–Pt–N bond angles are all close to 90°, such that the molecule is essentially a square planar complex that has a tetragonal distortion along one planar axis. This clearly can be attributed to residual sdσ-hybridization, as shown by examining the SOMO, which is bonding between the two short Pt–N bonds and antibonding between the two long Pt–N bonds. The fourth bond is undoubtedly weaker than the third because of larger steric repulsion between the NH_3 ligands and because of increasing electron density on the Pt^+ center.

The structures of the $x = 3$ and 4 complexes can also be examined from the viewpoint of ligand field theory [91]. The $Pt^+(NH_3)_4$ complex is a four-coordinate 17 e^- species. If this complex were to adopt a tetrahedral geometry, it would have a $(e_g)^4(t_{2g})^5$ electron configuration, clearly leading to distortion. By going to a square planar geometry (*xy* plane), the singly occupied orbital becomes the $d_{x^2-y^2}$ orbital, which points at the ligands. If this were a d^8 complex (instead of d^9) and the $d_{x^2-y^2}$ were unoccupied, the square planar geometry would be favored. However, single occupation of the $d_{x^2-y^2}$ apparently leads to the in-plane tetragonal distortion, which removes the degeneracy of the *x* and *y* directions and presumably allows the $d_{x^2-y^2}$, d_{z^2}, and s orbitals to mix to optimize the bonding by utilizing sd-hybridization. Upon removal of a ligand to form $Pt^+(NH_3)_3$, a 15 e^- complex, still d^9, is formed. Similar considerations as for the 4-coordinate complex hold and the ML_3 complex retains the near-square planar (T-geometry). Walsh diagrams for tri-coordinate complexes show that distortion towards a trigonal planar geometry are disfavored for a d^9 configuration because even though this distortion stabilizes the $d_{x^2-y^2}$ orbital, it strongly destabilizes the d_{xy} [91].

4.2. Comparison with the first row congener, $Ni^+(NH_3)_x$

Like the $Pt^+(NH_3)_x$ system, the first and second NH_3 ligands in $Ni^+(NH_3)_x$ are bound much more strongly than the third and fourth (Fig. 6) [37]. This trend is easily rationalized because Ni^+ has a $^2D(3d^9)$ ground state similar to the $^2D(5d^9)$ ground state of Pt^+. The ground electronic states of $Ni(NH_3)_x^+$ ($x = 1$–2) have been calculated to have doublet spin [88], and the $x = 3$ and 4 complexes almost certainly do as well. Thus, no spin changes are required as NH_3 molecules are successively added to Ni^+ to form $Ni^+(NH_3)_x$, just as for $Pt^+(NH_3)_x$ systems. In the nickel system, 4s–3dσ-hybridization is responsible for the strong bonding between Ni^+ and the first and second NH_3 ligands [34]. The first bond is actually weaker than the second because the energetic

costs of sd-hybridization are more severe for a single ligand.

It is interesting that the bonds to the first and second NH_3 ligands are stronger to Pt^+ than to Ni^+. This is somewhat surprising as one might anticipate that the heavier ion would be larger and therefore have longer metal–ligand bond distances, resulting in weaker bonds. We attribute the strong bonding in Pt^+ complexes to the lanthanide contraction and relativistic effects, which make the 6s orbital close in size to the 5d orbitals [92–94]. This leads to more efficient sdσ-hybridization for the platinum system and thereby a stronger electrostatic interaction between Pt^+ and the NH_3 ligand. This also leads to the observation that the first bond is stronger than the second in the $Pt^+(NH_3)_x$ system, in contrast to $Ni^+(NH_3)_x$. As some of the advantage of sd-hybridization is lost upon further ligation, the bond energies to Ni^+ become slightly larger for the $x = 3$ complex but then are comparable for $x = 4$. Overall, it appears that the influence of the lanthanide contraction and relativistic effects persist through the first solvation shell of four ligands.

4.2.1. Comparison with platinum carbonyls

The general trends in the sequential BDEs observed for $Pt^+(NH_3)_x$ complexes are also observed for platinum carbonyl cations, $Pt^+(CO)_x$ ($x = 1$–4) [37] (Fig. 6). This is clearly a consequence of the importance of sdσ-hybridization in both types of complexes. Previously, we examined periodic trends in the bonding of NH_3 and CO to the first row transition metal ions [34]. We found that the first two NH_3 BDEs are much larger than those to CO, just as they are for the Pt^+ complexes. This difference is attributed to the larger dipole moment and polarizability of NH_3, 1.47 D and 2.16 $Å^3$, compared to CO, 0.1 D and 1.94 $Å^3$ [95], such that the electrostatic interactions are larger. A reviewer notes that this trend can also be understood by examining the highest occupied and lowest unoccupied molecular orbitals (HOMOs and LUMOs) of these components. Namely, the ionization energies of Pt, NH_3, and CO are 9.0, 10.07, and 14.01 eV, respectively [96]. Thus, mixing of the orbitals (and the extent of charge transfer) on Pt^+ and NH_3 will be greater because the energy gap between the LUMO on Pt^+ and HOMO on NH_3 is only 1.1 eV compared to those for Pt^+ and CO, where the gap is 5.0 eV. Similar arguments hold for the first row congener, IE(Ni) = 7.64 eV [96].

Interestingly, the third and fourth ammonia BDEs to the first row metal ions are generally weaker than those for CO complexes, an observation also true for the Pt^+ complexes. This difference was attributed to two factors. First, the same properties that make the first two ammonia ligands bind strongly can also lead to stronger ligand–ligand repulsions that become increasingly important as more ligands are added to the complex. Second, in the CO case, π-backbonding interactions can enhance the bond energies, whereas ammonia does not engage in substantial π-interactions with the metal.

5. Conclusion

We report systematic measurements of the collision-induced dissociation of $Pt^+(NH_3)_x$ ($x = 1$–4) ions with Xe using guided-ion beam tandem mass spectrometry. From the thresholds for these processes, bond dissociation energies at 0 K are determined for Pt^+–NH_3, $(NH_3)Pt^+$–NH_3, $(NH_3)_2Pt^+$–NH_3, and $(NH_3)_3Pt^+$–NH_3 (Tables 2 and 4). The trend in the sequential bond energies of $Pt^+(NH_3)_x$ ($x = 1$–4) are discussed and compared with theoretical values, isovalent $Ni^+(NH_3)_x$ systems, and the related $Pt^+(CO)_x$ systems. The trends in sequential BDEs are explained in terms of sdσ-hybridization at the central metal ion, electrostatic interactions, and ligand–ligand steric interactions. Larger bond energies for platinum ammonia cations ($x = 1$ and 2) vs. nickel ones are attributed to more efficient sdσ-hybridization, a consequence of the lanthanide contraction and relativistic effects. A comparison of BDEs of platinum ammonia ions to those of platinum carbonyl ions illustrates that sdσ-hybridization is effective in both complexes and that the latter also involve some π-backbonding interactions.

Acknowledgements

M.L.S. acknowledges the award of a Melbourne University Abroad Traveling Scholarship and an APA Commonwealth Postgraduate Scholarships. This work was supported by the National Science Foundation under Grant CHE-0135517.

References

[1] D.P. Bamcroft, C.A. Lepre, S.J. Lippard, J. Am. Chem. Soc. 112 (1990) 6860.
[2] K.W. Jennette, T.J. Gill, J.A. Sadownick, S.J. Lippard, J. Am. Chem. Soc. 98 (1976) 6159.
[3] J. Reedijk, Inorg. Chim. Acta 198 (1992) 873.
[4] J. Reedijk, Chem. Commun. (1996) 801.
[5] W.I. Sundquist, S.J. Lippard, Coord. Chem. Rev. 100 (1990) 293.
[6] E. Wong, C.M. Giandomenico, Chem. Rev. 99 (1999) 2451.
[7] B. Lippert, Cisplatin: Chemistry and Biochemistry of a Leading Anticancer Drug, Wiley-VCH, Weinheim, 1999.
[8] S.E. Miller, D.A. House, Inorg. Chim. Acta 166 (1989) 189.
[9] S.E. Miller, D.A. House, Inorg. Chim. Acta 161 (1989) 131.
[10] S.E. Miller, D.A. House, Inorg. Chim. Acta 173 (1990) 53.
[11] H.C. Ehrsson, I.B. Wallin, A.S. Andersson, P.O. Edlund, Anal. Chem. 67 (1995) 3608.
[12] L.B. Martin, A.F. Schreiner, R.B. van Breemen, Anal. Biochem. 193 (1991) 6.
[13] T.G. Appleton, J.W. Connor, J.R. Hall, P.D. Prenzler, Inorg. Chem. 28 (1989) 2030.
[14] T.G. Appleton, J.R. Hall, S.F. Ralph, Inorg. Chem. 24 (1985) 673.
[15] R.E. Norman, J.D. Ranford, P.J. Sadler, Inorg. Chem. 31 (1992) 877.
[16] K.J. Barnham, M.I. Djuran, P.D.S. Murdoch, J.D. Ranford, P.J. Sadler, J. Chem. Soc. Dalton Trans. (1995) 3721.
[17] N. Xu, L. Pasa-Tolic, R.D. Smith, S. Ni, B.D. Thrall, Anal. Biochem. 272 (1999) 26.
[18] N. Tokuchi, H. Isobe, H. Takekawa, T. Hanada, T. Ishida, S. Ogura, K. Itoh, M. Furudate, K. Saito, Y. Kawakami, Br. J. Cancer 77 (1998) 1363.
[19] M.B.G. Kloster, J.C. Hannis, D.C. Muddiman, N. Farrell, Biochemistry 38 (1999) 14731.
[20] R. Romeo, Comments Inorg. Chem. 11 (1990) 21.
[21] D. Gibson, C.E. Costello, Eur. Mass Spectrom. 5 (1999) 501.
[22] R. Gupta, A. Kapur, J.L. Beck, M.M. Sheil, Rapid Commun. Mass Spectrom. 15 (2001) 2472.
[23] J.L. Beck, M.L. Colgrave, S.F. Ralph, M.M. Sheil, Mass Spectrom. Rev. 20 (2001) 61.
[24] M.L. Styles, Ph.D. Thesis, University of Melbourne, 2001.
[25] M.L. Styles, R.A.J. O'Hair, W.D. McFadyen, Eur. Mass Spectrom. 7 (2001) 69.
[26] K.J. Miller, E.R. Taylor, A. Basch, M. Krauss, W.J. Stevens, Biomol. Struct. Dyn. 2 (1985) 1157.
[27] P. Carloni, W. Andreoni, J. Hutter, A. Curioni, P. Gianozzi, M. Parrinello, Chem. Phys. Lett. 234 (1995) 50.
[28] A. Basch, M. Krauss, W.J. Stevens, D. Cohen, Inorg. Chem. 24 (1985) 3313.
[29] P. Car, M. Parrinello, Phys. Rev. Lett. 55 (1985) 2471.
[30] T.W. Hambley, Inorg. Chem. 14 (1992) 1.
[31] P. Carloni, M. Sprik, W. Andreoni, J. Phys. Chem. B 104 (2000) 823.
[32] P.N.V. Pavankumar, P. Seetharamulu, S. Yao, J.D. Saxe, D.G. Reddy, F.H. Hausheer, J. Comput. Chem. 20 (1999) 36.
[33] J.V. Burda, J. Sponer, J. Leszczynski, J. Biol. Inorg. Chem. 5 (2000) 178.
[34] D. Walter, P.B. Armentrout, J. Am. Chem. Soc. 120 (1998) 3176.
[35] P.J. Marinelli, R.R. Squires, J. Am. Chem. Soc. 111 (1989) 4101.
[36] P.M. Holland, A.W. Castleman, J. Chem. Phys. 76 (1982) 4195.
[37] X.-G. Zhang, P.B. Armentrout, Organometallics 20 (2001) 4266.
[38] R.H. Schultz, P.B. Armentrout, Int. J. Mass Spectrom. Ion Process. 107 (1991) 29.
[39] S.K. Loh, D.A. Hales, L. Lian, P.B. Armentrout, J. Chem. Phys. 90 (1989) 5466.
[40] E. Teloy, D. Gerlich, Chem. Phys. 4 (1974) 417.
[41] D. Gerlich, Adv. Chem. Phys. 82 (1992) 1.
[42] K.M. Ervin, P.B. Armentrout, J. Chem. Phys. 83 (1985) 166.
[43] P.J. Chantry, J. Chem. Phys. 55 (1971) 2746.
[44] E.R. Fisher, P.B. Armentrout, J. Chem. Phys. 94 (1991) 1150.
[45] P.B. Armentrout, in: N.G. Adams, L.M. Babcock (Eds.), Advances in Gas Phase Ion Chemistry, JAI Press, Greenwich, 1992, p. 83.
[46] M.T. Rodgers, P.B. Armentrout, J. Phys. Chem. A 101 (1997) 1238.
[47] F.A. Khan, D.E. Clemmer, R.H. Schultz, P.B. Armentrout, J. Phys. Chem. 97 (1993) 7978.
[48] N.F. Dalleska, K. Honma, P.B. Armentrout, J. Am. Chem. Soc. 115 (1993) 12125.
[49] N.F. Dalleska, K. Honma, L.S. Sunderlin, P.B. Armentrout, J. Am. Chem. Soc. 116 (1994) 3519.
[50] X.-G. Zhang, R. Liyanage, P.B. Armentrout, J. Am. Chem. Soc. 123 (2001) 5563.
[51] R.H. Schultz, K.C. Crellin, P.B. Armentrout, J. Am. Chem. Soc. 113 (1991) 8590.
[52] S.K. Loh, L. Lian, D.A. Hales, P.B. Armentrout, J. Chem. Phys. 89 (1988) 610.
[53] D.A. Hales, L. Lian, P.B. Armentrout, Int. J. Mass Spectrom. Ion Process. 102 (1990) 269.
[54] K. Ervin, S.K. Loh, N. Aristov, P.B. Armentrout, J. Phys. Chem. 87 (1983) 3593.
[55] D. Walter, M.R. Sievers, P.B. Armentrout, Int. J. Mass Spectrom. 173 (1998) 93.
[56] D.A. Hales, P.B. Armentrout, J. Cluster Sci. 1 (1990) 127.
[57] F. Muntean, P.B. Armentrout, J. Chem. Phys. 115 (2001) 1213.
[58] W.A. Chupka, in: J.L. Franklin (Ed.), Ion–Molecule Reactions, Plenum, New York, 1972, p. 33.

[59] W.J. Chesnavich, M.T. Bowers, J. Phys. Chem. 83 (1979) 900.
[60] P.B. Armentrout, Int. J. Mass Spectrom. Ion Process. 200 (2000) 219.
[61] T.S. Beyer, D.F. Swinehart, Commun. Assoc. Comput. Machinery 16 (1973) 379.
[62] S.E. Stein, B.S. Rabinovich, J. Chem. Phys. 58 (1973) 2438.
[63] S.E. Stein, B.S. Rabinovich, Chem. Phys. Lett. 49 (1977) 183.
[64] R.G. Gilbert, S.C. Smith, Theory of Unimolecular and Recombination Reactions, Blackwell Scientific, London, 1990.
[65] P.B. Armentrout, B.L. Kickel, in: B.S. Freiser (Ed.), Organometallic Ion Chemistry, Kluwer Academic Publishers, Dordrecht, 1996, p. 1.
[66] M.T. Rodgers, K.M. Ervin, P.B. Armentrout, J. Chem. Phys. 106 (1997) 4499.
[67] R.A. Marcus, O.K. Rice, J. Phys. Colloid Chem. 55 (1951) 894.
[68] R.A. Marcus, J. Chem. Phys. 20 (1952) 359.
[69] E.V. Waage, B.S. Rabinovitch, Chem. Rev. 70 (1970) 377.
[70] P.B. Armentrout, J. Simons, J. Am. Chem. Soc. 114 (1992) 8627.
[71] D.V. Dearden, K. Hayashibara, J.L. Beauchamp, N.J. Kirchner, P.A.M. van Koppen, M.T. Bowers, J. Am. Chem. Soc. 111 (1989) 2401.
[72] D.R. Salahub, in: K.P. Lawley (Ed.), Adv. Chem. Phys., Wiley, New York, 1987, p. 447.
[73] R.G. Parr, W. Yang, Density-Functional Theory of Atoms and Molecules, Oxford University Press, New York, 1989.
[74] A.D. Becke, J. Chem. Phys. 98 (1993) 5648.
[75] C. Lee, W. Yang, R.G. Parr, Phys. Rev. B 37 (1988) 785.
[76] M.J. Frisch, G.W. Trucks, H.B. Schlegel, G.E. Scuseria, M.A. Robb, J.R. Cheeseman, V.G. Zakrzewski, J.A. Montgomery Jr., R.E. Stratmann, J.C. Burant, S. Dapprich, J.M. Millam, A.D. Daniels, K.N. Kundin, M.C. Strain, O. Farkas, J. Tomasi, V. Barone, M. Cossi, R. Cammi, B. Mennucci, C. Pomelli, C. Adamo, S. Clifford, J. Ochterski, G.A. Petersson, P.Y. Ayala, Q. Cui, K. Morokuma, D.K. Malick, A.D. Rabuck, K. Raghavachari, J.B. Foresman, J. Cioslowski, J.V. Ortiz, B.B. Stefanov, G. Liu, A. Liashenko, P. Piskorz, I. Komaromi, R. Gomperts, R.L. Martin, D.J. Fox, T. Keith, M.A. Al-Laham, C.Y. Peng, A. Nanayakkara, C. Gonzalez, M. Challacombe, P.M.W. Gill, B. Johnson, W. Chen, M.W. Wong, J.L. Andres, C. Gonzalez, M. Head-Gordon, E.S. Replogle, J.A. Pople, GAUSSIAN 98, Revision A.7, in: Pople (Ed.), Gaussian, Inc., Pittsburgh, PA, 1998.
[77] A.P. Scott, L. Radom, J. Phys. Chem. 100 (1996) 16502.
[78] P.J. Hay, W.R. Wadt, J. Chem. Phys. 82 (1985) 299.
[79] J.B. Foresman, A.E. Frisch, Exploring Chemistry with Electronic Structure Methods, Gaussian, Inc., Pittsburgh, PA, 1996.
[80] C.E. Moore, NSRDS-NBS 35, vol. III, 1971, p. 1.
[81] F. Meyer, Y.-M. Chen, P.B. Armentrout, J. Am. Chem. Soc. 117 (1995) 4071.
[82] P.B. Armentrout, M.T. Rodgers, J. Phys. Chem. A 104 (2000) 2238.
[83] P.B. Armentrout, Acc. Chem. Res. 28 (1995) 430.
[84] M.T. Rodgers, P.B. Armentrout, Mass Spectrom. Rev. 19 (2000) 215.
[85] C.W. Bauschlicher, S.R. Langhoff, H. Partridge, in: B.S. Freiser (Ed.), Organometallic Ion Chemistry, Kluwer Academic Publishers, Dordrecht, 1996, p. 47.
[86] L.A. Barnes, M. Rosi, C.W. Bauschlicher, J. Chem. Phys. 93 (1990) 609.
[87] C.W. Bauschlicher, S.R. Langhoff, H. Partridge, J. Chem. Phys. 94 (1991) 2068.
[88] S.R. Langhoff, C.W. Bauschlicher, H. Partridge, M. Sodupe, J. Phys. Chem. 95 (1991) 10677.
[89] C.W. Bauschlicher, P.J. Maitre, J. Phys. Chem. 99 (1995) 3444.
[90] C.L. Haynes, P.B. Armentrout, J.K. Perry, W.A. Goddard III, J. Phys. Chem. 99 (1995) 6340.
[91] T.A. Albright, J.K. Burdett, M.H. Whangbo, Orbital Interactions in Chemistry, Wiley, New York, 1985.
[92] G. Ohanessian, M.J. Brusich, W.A. Goddard III, J. Am. Chem. Soc. 112 (1990) 7179.
[93] K.K. Irikura, J.L. Beauchamp, J. Phys. Chem. 95 (1991) 8344.
[94] K.K. Irikura, W.A. Goddard III, J. Am. Chem. Soc. 116 (1994) 8733.
[95] E.W. Rothe, R.B. Bernstein, J. Chem. Phys. 31 (1959) 1619.
[96] S.G. Lias, Ionization Energy Evaluation in NIST Chemistry WebBook, P.J. Linstrom, W.G. Mallard (Eds.), National Institute of Standards and Technology, Gaithersburg, MD, 2001, http://webbook.nist.gov.